Millimeter-long fiber Fabry-Perot cavities

Konstantin Ott,[1,2] **Sebastien Garcia,**[1] **Ralf Kohlhaas,**[2] **Klemens Schüppert,**[3] **Peter Rosenbusch,**[2] **Romain Long,**[1] **and Jakob Reichel**[1,*]

[1]*Laboratoire Kastler Brossel, ENS-PSL/CNRS/UPMC-Sorbonne Universités/CdF, 24 Rue Lhomond, 75005 Paris, France*
[2]*LNE-SYRTE, Observatoire de Paris, CNRS/UPMC-Sorbonne Universités, 61 Av. de l'Observatoire, 75014 Paris, France*
[3]*Institut für Experimentalphysik, Universität Innsbruck, Technikerstraße 25, 6020 Innsbruck, Austria*
[*]*jakob.reichel@ens.fr*

Abstract: We demonstrate fiber Fabry-Perot (FFP) cavities with concave mirrors that can be operated at cavity lengths as large as 1.5 mm without significant deterioration of the finesse. This is achieved by using a laser dot machining technique to shape spherical mirrors with ultralow roughness and employing single-mode fibers with large mode area for good mode matching to the cavity. Additionally, in contrast to previous FFPs, these cavities can be used over an octave-spanning frequency range with adequate coatings. We also show directly that shape deviations caused by the fiber's index profile lead to a finesse decrease as observed in earlier attempts to build long FFP cavities, and show a way to overcome this problem.

OCIS codes: (060.2310) Fiber optics; (120.2230) Fabry-Perot; (020.0020) Atomic and molecular physics; (230.3990) Micro-optical devices; (270.0270) Quantum optics.

References and links

1. Y. Colombe, T. Steinmetz, G. Dubois, F. Linke, D. Hunger, and J. Reichel, "Strong atom-field coupling for Bose-Einstein condensates in an optical cavity on a chip," Nature **450**, 272–276 (2007).
2. D. Hunger, T. Steinmetz, Y. Colombe, C. Deutsch, T. W. Hänsch, and J. Reichel, "A fiber Fabry-Perot cavity with high finesse," New J. Phys. **12**, 065038 (2010).
3. C. Toninelli, Y. Delley, T. Stöferle, A. Renn, S. Götzinger, and V. Sandoghdar, "A scanning microcavity for in-situ control of single-molecule emission," Appl. Phys. Lett. **97**, 021107 (2010).
4. M. Steiner, H. M. Meyer, C. Deutsch, J. Reichel, and M. Köhl, "Single ion coupled to an optical fiber cavity," Phys. Rev. Lett. **110**, 043003 (2013).
5. R. Albrecht, A. Bommer, C. Deutsch, J. Reichel, and C. Becher, "Coupling of a single nitrogen-vacancy center in diamond to a fiber-based microcavity," Phys. Rev. Lett. **110**, 243602 (2013).
6. M. Miguel-Sánchez, A. Reinhard, E. Togan, T. Volz, A. Imamoğlu, B. Besga, J. Reichel, and J. Estève, "Cavity quantum electrodynamics with charge-controlled quantum dots coupled to a fiber Fabry-Perot cavity," New J. Phys. **15**, 045002 (2013).
7. B. Besga, C. Vaneph, J. Reichel, J. Estève, A. Reinhard, J. Miguel-Sánchez, A. Imamoğlu, and T. Volz, "Polariton boxes in a tunable fiber cavity," Phys. Rev. Appl. **3**, 014008 (2015).
8. N. E. Flowers-Jacobs, S. W. Hoch, J. C. Sankey, A. Kashkanova, A. M. Jayich, C. Deutsch, J. Reichel, and J. G. E. Harris, "Fiber-cavity-based optomechanical device," Appl. Phys. Lett. **101**, 221109 (2012).
9. B. Petrak, N. Djeu, and A. Muller, "Purcell-enhanced Raman scattering from atmospheric gases in a high-finesse microcavity," Phys. Rev. A **89**, 023811 (2014).
10. M. Mader, J. Reichel, T. W. Hänsch, and D. Hunger, "A scanning cavity microscope," Nature Comm. **6**, 7249 (2015).
11. B. Brandstätter, A. McClung, K. Schuppert, B. Casabone, K. Friebe, A. Stute, P. O. Schmidt, C. Deutsch, J. Reichel, R. Blatt, and T. E. Northup, "Integrated fiber-mirror ion trap for strong ion-cavity coupling," Rev. Sci. Instrum. **84**, 123104 (2013).

#261274 Received 16 Mar 2016; revised 17 Apr 2016; accepted 18 Apr 2016; published 27 Apr 2016

12. H. Takahashi, J. Morphew, F. Oručević, A. Noguchi, E. Kassa, and M. Keller, "Novel laser machining of optical fibers for long cavities with low birefringence," Opt. Express **22**, 31317 (2014).
13. R. Szmuk, V. Dugrain, V. Maineult, J. Reichel, and P. Rosenbusch, "Stability of a trapped-atom clock on a chip," Phys. Rev. A **92**, 012106 (2015).
14. I. D. Leroux, M. H. Schleier-Smith, and V. Vuletić, "Orientation-dependent entanglement lifetime in a squeezed atomic clock," Phys. Rev. Lett. **104**, 250801 (2010).
15. O. Hosten, N. J. Engelsen, R. Krishnakumar, and M. A. Kasevich, "Measurement noise 100 times lower than the quantum-projection limit using entangled atoms," Nature **529**, 505 (2016).
16. C. M. Miller and F. J. Janniello, "Passively temperature-compensated fibre Fabry-Perot filter and its application in wavelength division multiple access computer network," Electron. Lett. **26**, 2122 (1990).
17. See for example www.micronoptics.com.
18. J. Benedikter, T. Hümmer, M. Mader, B. Schlederer, J. Reichel, T. W. Hänsch, and D. Hunger, "Transverse-mode coupling and diffraction loss in tunable Fabry-Pérot microcavities," New J. Phys. **17**, 053051 (2015).
19. M. Uphoff, M. Brekenfeld, G. Rempe, and S. Ritter, "Frequency splitting of polarization eigenmodes in microscopic Fabry-Perot cavities," New J. Phys. **17**, 013053 (2015).
20. D. Hunger, C. Deutsch, R. J. Barbour, R. J. Warburton, and J. Reichel, "Laser micro-fabrication of concave, low-roughness features in silica," AIP Adv. **2**, 012119 (2012).
21. T. A. Birks, J. C. Knight, and P. S. J. Russell, "Endlessly single-mode photonic crystal fiber," Opt. Lett. **22**, 961–963 (1997).
22. W. B. Joyce and B. DeLoach, "Alignment of Gaussian beams," Appl. Opt. **23**, 4187–4196 (1984).
23. In principle, this problem can be overcome by the use of time-reversal techniques to achieve the desired mode at the output of the multimode fiber. However, a suitable scheme to obtain an error signal remains to be found.
24. I. N. Papadopoulos, S. Farahi, C. Moser, and D. Psaltis, "High-resolution, lensless endoscope based on digital scanning through a multimode optical fiber," Biomed. Opt. Express **4**, 260 (2013).
25. Newport GTS150 and GTS30V, Attocube ECS5050NUM.
26. Nikon CF IC EPI Plan DI 20×.
27. J. Schmit and J. Creath, "Extended averaging technique for derivation of error-compensating algorithms in phase-shifting interferometry," Appl. Opt. **34**, 3610 (1995).
28. Nyfors Autocleaver.
29. Y. Colombe, D. H. Slichter, A. C. Wilson, D. Leibfried, and D. J. Wineland, "Single-mode optical fiber for high-power, low-loss UV transmission," Opt. Express **22**, 19783 (2014).
30. Laseroptik GmbH, Garbsen, Germany.
31. J. Degallaix, "OSCAR, a Matlab-based optical FFT code," J. Phys.: Conf. Ser. **228**, 012021 (2010).
32. A. Roy and M. D. Barrett, "Fabrication of glass micro-cavities for cavity quantum electrodynamics experiments," Appl. Phys. Lett. **99**, 171112 (2011).

1. Introduction

Fiber Fabry-Perot (FFP) microcavities with CO_2 laser-machined concave mirrors [1, 2] are being used in a fast-growing number of applications, ranging from cavity quantum electrodynamics with atomic, molecular and solid-state emitters [1, 3–7] and optomechanical systems [8] to Raman spectrometers for atmospheric gases [9] and new scanning microscopy techniques [10]. This range of applications could be further increased, and a gap in micro-optical technology could be filled, by increasing the optical length L of these cavities to the millimeter range while maintaining their crucial advantages such as built-in fiber coupling, small mode waist, high finesse and high passive stability. Development towards this goal has been initiated by the ion trap community [11, 12], where FFP cavities are now arguably the most promising candidate for realizing a high-fidelity light-matter quantum interface. In this application, increased cavity length will mitigate or even remove the perturbation of the trapping potential induced by the dielectric mirrors. With neutral atoms, increased mirror distance will allow elongated atomic ensembles to be placed in the cavity, as required for improving compact, trapped-atom atomic clocks [13] by cavity squeezing [14, 15]. Finally, because of the reduced free spectral range, larger L will also make it possible to use laser-machined concave mirrors in telecom applications of FFP cavities, where planar mirrors [16] are currently being used in commercial solutions [17].

Two factors have limited L in earlier FFP implementations. First, the nonspherical profile generated by a single CO_2 laser pulse causes additional losses which are negligible for short

#261274 Received 16 Mar 2016; revised 17 Apr 2016; accepted 18 Apr 2016; published 27 Apr 2016

cavities, but become important long before L reaches the stability limit [2,11,12,18]. The Gaussian rather than spherical shape [2] limits the effective mirror diameter, even when a very large CO_2 beam diameter is used [19]. Shape deviations due to the doping of the fiber core [12] and to the restricted heat flow in the fiber [20] also contribute to this limitation. Second, because FFPs have no mode-matching optics, the mode field diameter of the fiber determines the coupling efficiency between the fiber and cavity mode. With typical mirror curvatures, the standard single-mode (SM) fibers used in earlier FFP implementations provide near-perfect mode matching to short cavities, and are used with great success in cavity quantum electrodynamics experiments. Resonant cavity transmission T_c rapidly drops, however, when L is increased beyond a few hundred μm [2, 11].

Concerning the mirror profile, a natural approach is to use multiple CO_2 laser pulses on the same fiber, instead of a single pulse. A first application of this approach was demonstrated recently in [12], where the fiber was rotated about its axis between pulses. The main purpose of this rotation was to reduce mirror ellipticity, but the technique also resulted in larger mirror profiles, enabling values of L up to $400\,\mu$m before the finesse dropped by 50%, for cavities with one SM fiber. However, the mirror profile still remained Gaussian and the problem of reduced transmission remained unsolved.

Here, we overcome both limitations. To address the mirror shape limitation, we apply a newly developed CO_2 dot milling technique, where a large number of weak individual pulses sequentially address an optimized pattern of target points on the substrate surface. This method gives access to a wide range of shapes with extremely precise control over the surface profile, while maintaining the excellent surface roughness that is characteristic of CO_2 machining. Here we show that it enables fabrication of large, spherical structures, as required for long cavities, with a shape deviation of less than $\lambda/20$. To address the mode-matching issue, we use large-mode-area photonic-crystal (PC) fibers, also known as "endlessly single-mode" fibers [21]. We find that CO_2 machining produces excellent results on these fibers when the holes are collapsed adequately. To measure the performance of the improved mirrors, we have built cavities and performed finesse and transmission measurements. $L > 1.6\,$mm is reached before the finesse drops by 50%. We present measurements of finesse as a function of L for different cavities and compare them to simulations that use the measured mirror profiles, finding good agreement. These simulations also clarify the impact of doping-related shape variations. We also measure cavity transmisson over the full length range and directly compare the results of a PC-multimode (MM) fiber cavity to a SM-MM cavity with similar mirror parameters. We find that the PC fiber improves the transmission by an order of magnitude for cavity lengths beyond 1 mm.

2. The role of the cavity mode radius on the fiber mirrors

The mode radius of the cavity mode on the mirrors plays an important role for both the losses and the mode matching. Limiting ourselves to symmetric cavities for simplicity, the mode radius on the cavity mirrors is $w_m = w_c\sqrt{1+(L/(2z_R))^2}$ where $w_c = \sqrt{\lambda/(2\pi)}(L(2R-L))^{1/4}$ is the waist radius of the cavity mode and $z_R = \pi w_c^2/\lambda$ its Rayleigh range, R is the radius of curvature (ROC) of the mirrors, L the cavity length, and λ the wavelength. A small w_m has the advantage of minimizing the clipping losses due to the finite mirror diameter (see Sec. 5 below). Additionally, for the long cavities that we are targeting here, w_m tends to be larger than the mode field radius of the input fiber, w_f. This reduces the power coupling efficiency ε from the fiber to the cavity, and consequently, the overall (fiber-to-fiber) resonant cavity transmission T_c. Here as well, reducing w_m is beneficial. The smallest w_m that can be reached for a given L

#261274 Received 16 Mar 2016; revised 17 Apr 2016; accepted 18 Apr 2016; published 27 Apr 2016

is realized for $R = L$, i.e., a confocal cavity. In that case,

$$w_{m,\min} = \sqrt{\frac{\lambda}{\pi} L} \;\; and \;\; w_c = \sqrt{\frac{\lambda}{2\pi} L}. \tag{1}$$

Taking $\lambda = 780\,\mathrm{nm}$ and $L = 1.2\,\mathrm{mm}$ for example, we find $w_{m,\min} = 17.3\,\mu\mathrm{m}$ and $w_c = 12.2\,\mu\mathrm{m}$. This is still much larger than the mode field radius of a typical SM fiber, so that a better solution must be found, as discussed further below.

The fiber-to-cavity power coupling efficiency can be approximated by the mode overlap of two Gaussian modes [22],

$$\varepsilon \approx \frac{4}{\left(\frac{w_f}{w_c} + \frac{w_c}{w_f}\right)^2 + \left(\frac{\lambda}{\pi w_f w_c}\right)^2 s^2}, \tag{2}$$

w_f being the waist radius of the mode entering the cavity from the fiber, w_c that of the cavity mode as before, and s the distance between the two waist positions. The lensing effect of the concave mirror structure, as well as the additional phase mismatch due to the wavefront curvature of the cavity mode can be neglected for the long FFPs considered here. (A treatment including these effects can be found in the appendix of [2].) For a symmetric cavity, $s = L/2$. We find it convenient to introduce the dimensionless factor

$$\alpha \equiv \frac{L}{2z_R} = \frac{1}{\sqrt{2\frac{R}{L} - 1}}, \tag{3}$$

such that $\alpha = 1$ for a confocal cavity, $\alpha \to 0$ for a short cavity, and $\alpha \to \infty$ when approaching the concentric limit $L = 2R$. The power coupling efficiency can then be written

$$\varepsilon = \frac{4}{\left(\frac{w_f}{w_c} + \frac{w_c}{w_f}\right)^2 + \left(\frac{w_c}{w_f}\right)^2 \alpha^2}, \tag{4}$$

which depends only on the ratio w_f/w_c and α.

Figure 1(a) shows this coupling efficiency for different α. The optimum coupling ε_{max} for a given α is reached for $w_f/w_c = \sqrt[4]{1+\alpha^2}$. For configurations with $0 \le \alpha \lesssim 1$, this corresponds to $1 \le w_f/w_c \lesssim 1.2$: for cavity lengths up to the confocal length, the optimum fiber mode radius is always close to the waist of the cavity mode. A coupling efficiency rigorously equal to 1 can only be reached for $\alpha = 0$, but high coupling efficiencies $\varepsilon > 0.8$ are possible for a wide range of α values, as shown in Fig. 1(b). Whether these efficiencies can actually be realized experimentally depends on the availability of a suitable fiber. For long cavities, we have already seen that w_m tends to be larger than typical fiber modes, and can also cause losses due to finite mirror diameter. Therefore, a good working point for these cavities is close to the confocal configuration $\alpha = 1$, where w_m is smallest. Note that further optimization is possible in situations where asymmetric cavities can be employed, notably for plano-concave configurations with asymmetric reflectivity.

3. Photonic-crystal fibers for FFP cavities

The discussion above shows that mode matching for long fiber cavities can be substantially improved by using a fiber with larger mode field diameter. It is known that large-core multimode fibers improve the transmission (see [12] for a direct comparison). However, the need for a well-defined, stable coupling usually makes them a bad choice on the input side of the cavity [23,24].

#261274 Received 16 Mar 2016; revised 17 Apr 2016; accepted 18 Apr 2016; published 27 Apr 2016

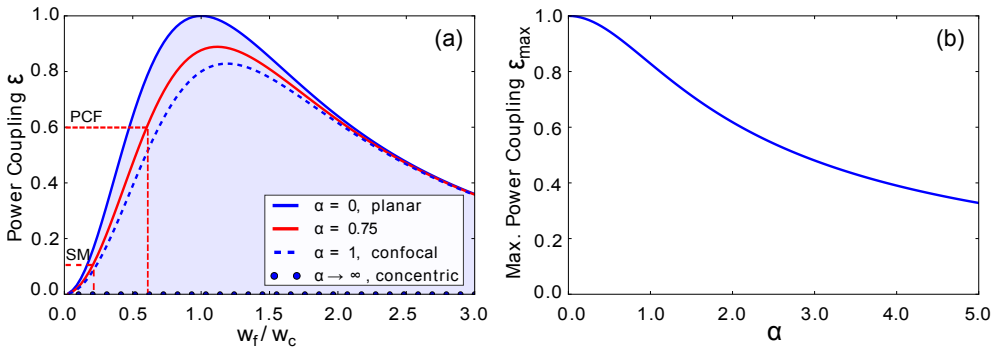

Fig. 1. (a) Power coupling between the incoupling fiber mode and the mode of a symmetric cavity for different values of α (the cavity length normalized to the Rayleigh range of the cavity mode). The red dashed lines indicate the increased power coupling expected from the use of a PC fiber ($w_f = 8.2\,\mu$m) with respect to a standard SM fiber ($w_f = 3\,\mu$m) for an example cavity with $w_0 = 14.1\,\mu$m and $L = 1.2$ mm. The blue shaded area shows the stability region of the symmetric cavity. (b) Maximum achievable power coupling for a given α.

A promising alternative, which we explore here, is to use single-mode fibers with large mode area. Such fibers are available based on different technologies. Here we use photonic-crystal (PC) fibers.

Let us evaluate the power coupling that can be expected for $L = 1.2$ mm, which is the targeted cavity length in our application. In practice, at the confocal point itself, stability is compromised by the fact that the mirror ROCs have some tolerance from sample to sample (see sec. 4.4 below), so we choose to work at $\alpha \sim 0.75$. The required ROC to realize a given combination (α, L) is $R = L/2\left(1/\alpha^2 + 1\right)$. For $L = 1.2$ mm and $\alpha = 0.75$, the required ROC is $R = 1.67$ mm. The calculated cavity mode waist for these parameters is $w_c = 14.1\,\mu$m at 780 nm. The red dashed lines in Fig. 1 show the expected power coupling efficiency of this mode to a standard SM fiber with $w_f = 3\mu$m, $\varepsilon \approx 11\%$, and to the NKT LMA20 photonic crystal fiber which we have used in our experiments, which has a specified near-field mode field radius of $w_f = (8.2 \pm 0.8)\mu$m at 780 nm (see Tab. 1 below for more information). This w_f value leads to $\varepsilon \approx 58\%$, nearly a factor 6 higher than with the SM fiber. Note however that this idealized calculation neglects effects such as the non-Gaussian shape of the PC fiber mode, so its result should be considered as an upper limit.

In addition to the improved mode coupling, these PC fibers are "endlessly single mode", allowing stable single-mode guiding over a large wavelength range which can span more than an octave. Here, we will use them with a dual-wavelength coating optimized for 780 nm and 1560 nm.

4. Machining large spherical structures by CO_2 dot milling

4.1. Limiting factors in single-pulse machining

The profile of the depression generated by a single CO_2 laser pulse is Gaussian rather than spherical [2], so that the effective mirror diameter is significantly smaller than the diameter of the depression. Additionally, due to boundary effects in heat transport during the laser machining, it is difficult to machine depressions that extend over the full fiber surface [20], even with a very large CO_2 beam diameter [19]. The small effective mirror size causes clipping loss when the transverse mode size on the mirror becomes comparable to the effective mirror diameter.

#261274 Received 16 Mar 2016; revised 17 Apr 2016; accepted 18 Apr 2016; published 27 Apr 2016

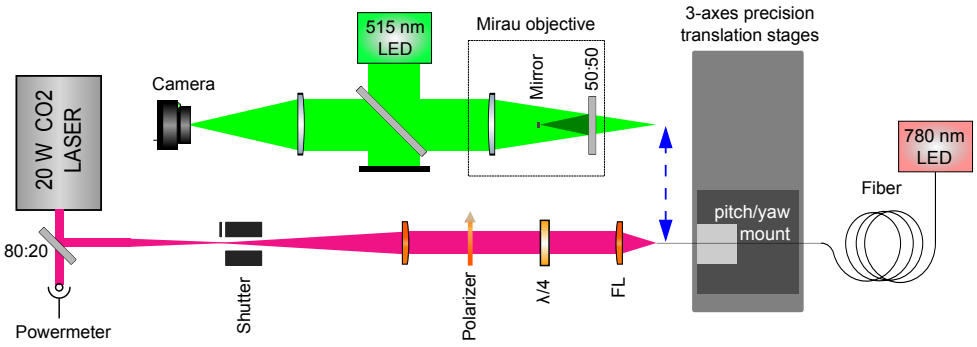

Fig. 2. CO_2 dot milling setup: Precision translation stages are used to control the CO_2 beam position on the fiber and to translate the fiber to the optical profiler position for surface characterization. Light coupled into the fiber core allows a precise centering of the mirror profile. The CO_2 focusing lens (FL) is a $f = 25$ mm asphere illuminated with a beam diameter of 7 mm.

This typically happens long before L reaches to the stability limit [2, 11, 12, 18]. Finally, it is known that the milling profile of a given laser pulse is affected by the doping profile of the fiber [12]. The effect is most pronounced for SM fibers, where it leads to a circular ridge at the core-cladding interface. All three problems can be addressed by replacing the single CO_2 pulse by a series of pulses with different target positions.

4.2. Dot milling setup

Our machining setup is designed to enable surface machining with multiple, precisely positioned CO_2 pulses ("shots") and analysis of the results on the fly. It has three main components: the CO_2 laser with external pulsing and focusing optics, a high-precision, three-axis translation stage, and an in-situ optical profilometer (Fig. 2). The complete setup is enclosed in a temperature-stabilized laminar flow box. A home-made motorized tilt stage (pitch and yaw) was mounted on the translation stages to align the fiber cleave surface perpendicular to the CO_2 beam axis before machining. The CO_2 part is similar to our earlier setups [2, 20]. Pulses are generated using a combination of pump switching and mechanical shutters [2]; pulse-to-pulse power fluctuations are on the order of 0.5%. The CO_2 focusing lens is a $f = 25$ mm asphere illuminated with a beam diameter of 7 mm. In contrast to [2, 20], however, the CO_2 and profilometry beam paths are kept separated, with the translation stages ensuring reproducible travel between the two locations. The stages [25] have optical encoders for repeatble absolute positioning. The step size of the transverse stages is 50 nm. The optical profilometer is based on a Mirau objective [26] with a nominal transverse resolution of 0.8 μm. To achieve best height (z) resolution, we use phase-shifting profilometry [27]. The measured noise for a reference surface is 1.4 nm rms for a single profile, which can be further reduced to the sub-nm level by averaging several profiles. To localize the fiber core of SM fibers, weak light is coupled into the fiber, so that the core appears as a bright spot on the microscope image. The whole system is software-controlled and allows for automated centering.

With this improved setup, the measured average centering error of a CO_2 shot with respect to the fiber core is 0.9 μm, which is a significant improvement over the earlier setup, and just sufficient to achieve reproducible mode-matching between the fiber and cavity modes. The remaining error has contributions from the translation stages (thermal drifts in particular), and possibly from the CO_2 laser's beam pointing stability. The relative positions of the multiple

#261274 Received 16 Mar 2016; revised 17 Apr 2016; accepted 18 Apr 2016; published 27 Apr 2016

shots making up the dot milling pattern have much better accuracy because they do not require the 4.5 cm translation between the profiler and the CO2 beam, which is needed in the centering procedure.

4.3. Fiber preparation

We have machined three different fiber types, presented in Table 1. For good reproducibility of the machining results, it is important to control the cleave angle to tight tolerances. We have used a pneumatic cleaver with a specified typical cleave angle of less than 0.3 degrees [28]. Our measured mean cleave angle deviation was less than 0.4 degrees throughout, and below 0.2 degrees for the SM fibers. To achieve these results, the cleaver has to be calibrated carefully and the copper-coated fibers have to be straightend by hand before cleaving. For the PC fiber, simple cleaving exposes the holes of the photonic crystal. We found that direct machining on that structure was possible for profiles with $R \lesssim 300\,\mu$m. For the much shallower profiles of our targeted $R > 1000\,\mu$m mirrors, this simple approach turned out to be problematic. Therefore, we have collapsed the holes before cleaving using the arc of a fusion splicer as described in Ref. [29]. The cleave was positioned at a distance $d_c \sim 50 - 100\,\mu$m from the onset of the collapsed region as shown in Fig. 3. Excellent results were achieved with the fibers prepared in that way. For shorter d_c, residues of the six-fold symmetry of the PC hole pattern remained visible in the machined structure.

Table 1. **Fiber Types Used in the Experiments**

Type	**Supplier**	**Ref.**	**MFD**[a]	**Wavelength range**	**Coating**
			μm	nm	
MM	IVG Fiber	Cu200/220 IR	200±3	700–1700	copper
SM	IVG Fiber	Cu800-200	6±0.5	800–1000	copper
PC	NKT Photonics	LMA 20	16.4±1.5	700–1700	acrylate

[a] The mode field diameter (MFD) indicated here is the nominal value specified by the manufacturer. The actual value depends on wavelength. For the MM fiber, the core diameter is specified instead of the MFD.

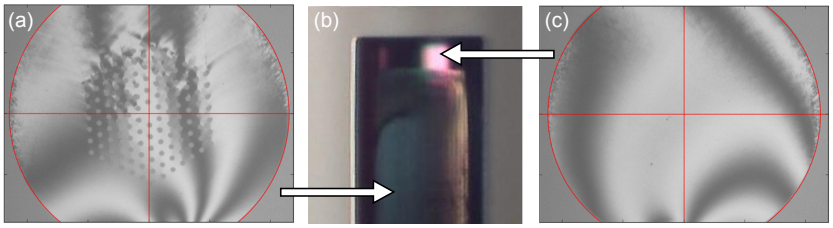

Fig. 3. (a) Profilometer image of the surface of a PC fiber (NKT LMA 20) cleaved in the non-collapsed region, indicated by the arrow. (b) Side view of a PC fiber, showing the transition between the non-collapsed and collapsed regions. (c) Profilometer image of the surface for a cleave in the collapsed region. (The red crosshairs in (a) and (c) mark the center of the fiber.)

#261274 Received 16 Mar 2016; revised 17 Apr 2016; accepted 18 Apr 2016; published 27 Apr 2016

4.4. *Optimizing the dot milling process*

Our fabrication goal was to obtain spherical mirror profiles with ROCs in the 1 mm range, and with a useful diameter of 100 μm. We have achieved good results using identical CO_2 beam parameters for all dots in the pattern. For the results shown below, the beam had a $1/e^2$ radius $w = 140\,\mu$m, and its power was $P = 2.3$ W. The pulse length τ was adjusted such that an individual milling pulse near the center of a flat (cleaved) MM fiber yielded a depression with depth $t \sim 100$ nm and diameter (2σ of a Gaussian fit) of $\sim 30\,\mu$m. This led to $17\,\text{ms} \leq \tau \leq 25\,\text{ms}$ depending on the fiber type. This dot size is small enough to produce features with the required resolution and using about one hundred pulses, while a smaller beam diameter would require more pulses with no obvious advantage.

The milling process is highly nonlinear, so that the time order of the pulses also affects the result. Furthermore, due to the finite size of the fiber, the effect of a given pulse also depends on its distance from the center of the fiber surface. Therefore, finding a suitable milling pulse pattern requires some empirical testing to reduce the parameter space before a systematic optimization can be done.

We have used the following strategy: because the desired shape has rotational symmetry, the milling pulses are placed on concentric circles. The outmost circles are shot first. The number of pulses is limited to ~ 100, because this range was empirically found to give good results and higher numbers brought no obvious improvements. To reduce effects of the shot order, neighboring pulse positions are not shot consecutively. The number and diameters of the circles are optimized experimentally by minimizing the difference between the measured profile and a spherical surface over a circular region of interest. A typical pulse pattern is shown in Fig. 4(a). Once the pattern is optimized, processing and characterizing a single fiber with a typical 75-dot pattern takes less than 2 minutes.

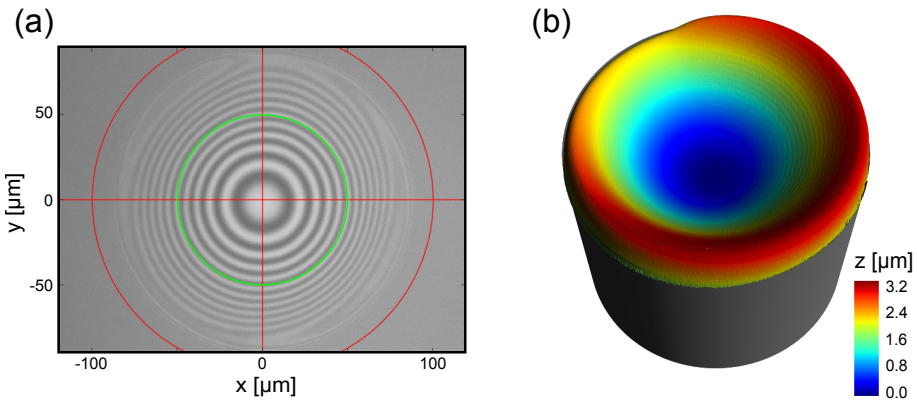

Fig. 4. Large spherical surface machined on a 200 μm diameter SM fiber. (a) Interferogram of the surface after processing. The red circle shows the initial fiber diameter, the green circle shows the area over which the structure was optimized. The crosshairs indicate the center of the fiber. The red dots indicate the positions of the CO_2 pulses (b) Surface profile measured by phase-shifting interferometry. (The grey area was added to indicate the fiber orientation.)

Using this type of pattern, we have produced mirror profiles on SM, MM and PC fibers. Figures 4 and 5 show sample results. The shot positions and parameters were optimized for $R = 1500\,\mu$m, where the mean deviation from a 2D spherical fit is smaller than 12 nm, and the maximum deviation smaller than 40 nm, over a circular region of interest with a diameter of 100 μm. Between samples processed with identical parameters, the measured R varies by

#261274 Received 16 Mar 2016; revised 17 Apr 2016; accepted 18 Apr 2016; published 27 Apr 2016

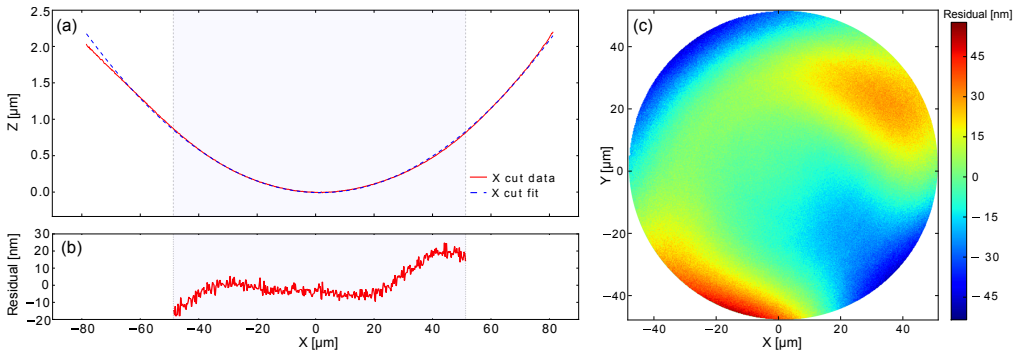

Fig. 5. (a) Cut along the x axis of a spherical profile on a 220 μm diameter MM fiber and corresponding cut of a two-dimensional spherical fit ($R = 1475\,\mu$m) on a circular region with a diameter of 100 μm. (The shaded area in (a) and (b) indicates the fit region.) (b) Cut along the x axis of the fit residuals. (c) 2D fit residuals.

about $\pm 10\,\%$ on SM and MM fibers, and by about $\pm 20\,\%$ on PC fibers. Within some limits, larger and smaller profiles can be machined by simply changing the pulse length and scaling the shot positions, without optimizing anew. When machining smaller R with the profile of Fig. 4, the mean deviation increases up to 59 nm for $R = 330\,\mu m$. When producing $R > 1500\,\mu$m the mean deviation does not increase significantly, but cleave imperfections start to compromise the symmetry of the structure. The ellipticity $R_a - R_b/R_a$ is below 10%, where R_a and R_b are the radii of the large and the small axis, respectively, of a 2D fit to the measured profile over a region of $100\,\mu$ diameter. This ellipticity could in principle be further reduced by adapting the milling pattern. However, ellipticity-induced birefringent splitting of the cavity resonance frequencies scales as $1/L$ [19], making it a small effect for the comparatively long cavities considered here. Therefore, we did not attempt such an optimization here.

With SM fibers, we also observe a shape deviation of 20-40nm height located near the interface between the cladding and doped core, similar to that reported in [12] for several pulses on the fiber center. It can be compensated to some extent by slight adjustments in the milling pattern, with the results shown in Fig. 6. Collapsed PC fibers do not experience this effect, which makes them particularly suitable for CO_2 processing. Likewise, large-core MM fibers are also easy to process because of their large, homogeneous central region.

5. Long fiber Fabry-Perot cavities

We have machined a large number of SM, MM and PC fibers and had them coated with an ion-beam sputtered (IBS), dual-wavelength high-reflectivity coating [30] for 780 nm and 1560 nm. (This particular coating was chosen as required for our application, where Rb atoms are trapped in a far off-resonant dipole trap inside the cavity.) Its nominal transmission is $\mathscr{T} = 30$ ppm at 780 nm and 1560 nm; the sum $\mathscr{T} + \mathscr{L}$ is 66 ± 2 ppm at 780 nm and 34 ± 2 ppm at 1560 nm, as determined from finesse measurements on short FFP cavities.

5.1. Finesse and transmission measurement

We have built high-finesse cavities from fiber pairs of different fiber types using a three-axis translation stage equipped with piezo actuators (Thorlabs MAX311D/M) and a two-axis rotation stage (Thorlabs PR01/M, GNL10/M). Several PC-MM cavities were tested at both wavelengths. Compared to cavities with the standard Gaussian-shaped fiber mirrors, the difference was striking. With mirror ROCs on the order of 1 mm, we could readily achieve stable cavities

#261274 Received 16 Mar 2016; revised 17 Apr 2016; accepted 18 Apr 2016; published 27 Apr 2016

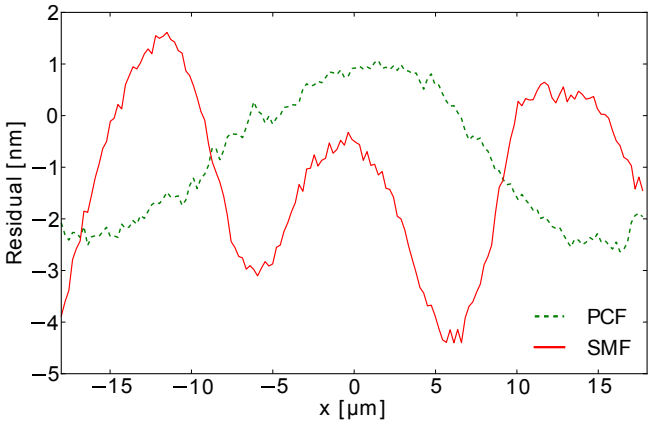

Fig. 6. Influence of the doped core region. Shown are the residuals of a 2D spherical fit for machined SM and PC fiber surfaces. The milling patterns are very similar for both fibers and are close to the one shown in Fig. 4(a). 73 pulses were used for the SM fiber and 70 for the PC fiber; the pulse length is $\tau = 17.6$ ms for the SM fiber and $\tau = 20$ ms for the PC fiber. The data is the average of 120 profile measurements for each fiber (see Sec. 5.3). The radius of the fit region was chosen to be 18 μm because this is the mode radius on the fiber for a cavity of length $L = 1200$ μm and a ROC $R = 1650$ μm. The fit for the PC fiber gives $R = 1492\mu$m and the residual shows only a slow modulation, which could probably be further reduced by fine-tuning the pulse length of the last, central pulse. By contrast, the residual of the standard SM fiber (fitted $R = 1508\mu$m) shows a strong variation at the fiber center at the interface between core an cladding material.

with sizeable transmission for lengths $L > 1$ mm – a length never achieved with the Gaussian-shaped mirrors (Fig. 7(a)).

The cavities performed well at both wavelengths, and the measured finesse values were consistent with the coating specifications. With traditional SM fibers, it would be impossible to use the same FFP cavity with wavelengths so far apart. The optical measurements presented below were performed using an external-cavity diode laser at 780 nm. The cavity length L was measured with a simple video microscope. The free spectral range (FSR) was calculated from L as $\nu_{\mathrm{FSR}} = c/2L$. The cavity length was then scanned around this position using the piezo. The linewidth $\delta\nu$ of the TEM_{00} mode was measured using an electro-optic modulator to generate sidebands for frequency calibration.

These measurements were repeated for different cavity lengths over the full stability range. Cavity transmission on resonance was also measured for every length. In order to eliminate the uncertainty associated with coupling a free-space beam into the cavity fiber, we have first injected the free-space beam into an open-ended fiber and measured the power emerging from the open end before splicing it to the mirror fiber. In this way, the uncertainty is only given by the splice. Based on previous splices, we estimate splice transmission to be $T_{splice} \gtrsim 0.97$ for SM fibers, and $T_{splice} \gtrsim 0.9$ for PC fibers. (The typical value for the PC case is closer to 0.95, but is very sensitive to all splice preparations, such as the cleave angle.)

Figure 7(b) and (c) show the finesse $\mathscr{F} = \nu_{\mathrm{FSR}}/\delta\nu$ and resonant transmission T_c measured at 780 nm as a function of cavity length for two different cavities: one with an SM fiber (ROC measured by optical profilometry: $R_1 = 1508 \pm 65\,\mu$m) on the incoupling side and a MM fiber ($R_2 = 1629 \pm 73\,\mu$m) for outcoupling; the other with the same MM fiber, but a PC fiber ($R_1 = 1492 \pm 110\,\mu$m) on the incoupling side. Because the ROCs are not exactly equal, an unstable

#261274 Received 16 Mar 2016; revised 17 Apr 2016; accepted 18 Apr 2016; published 27 Apr 2016

region exists for both cavities where $R_1 < L < R_2$. This is clearly visible in the finesse and transmission data. Comparing the performance of the two cavities, the PC-MM configuration is superior in every respect. It shows higher transmission, especially for large L. This was expected and validates the choice of the PC fiber, although the experimental values do not reach the theoretical optimum yet (see Sec. 5.4 below). Furthermore, with this cavity, $\mathscr{F}$ is almost constant up to $L \sim 1.5\,\mathrm{mm}$, whereas with the SM-MM cavity, it decreases significantly with L, even for short lengths. Such a decrease has been observed for all FFP cavities involving SM fibers [11, 12, 18]; the authors of [12] have conjectured that it is likely to be caused by the ridge in the mirror profile (cf. Fig. 6). We confirm this quantitatively using a numerical simulation that takes into account the measured mirror profile, as described below in Sec. 5.3. This adverse effect is virtually absent with PC fibers, giving them an additional advantage in FFP cavities.

5.2. *Analytical model: Clipping loss*

Clipping loss for Gaussian cavity modes can be described with a simple analytical model [2]. The finesse of a high-finesse Fabry-Perot cavity as a function of the mirror properties is

$$\mathscr{F} = \frac{2\pi}{\mathscr{L}_A + \mathscr{L}_S + \mathscr{L}_C + \mathscr{T}} \tag{5}$$

where $\mathscr{L}_A$ are the absorption losses in the coatings, $\mathscr{L}_S$ the scattering losses, $\mathscr{T}$ the transmissions, $\mathscr{L}_C$ the clipping losses, and each term is the sum of the contributions of the two mirrors. Since all our fiber mirrors were coated in the same run, and all substrates are CO_2-machined fused silica, we assume that all loss terms are the same for the two mirrors except for clipping loss. The latter depends on the effective mirror diameter D_i ($i = 1, 2$) and the mode field radius w_i on the mirror: $\mathscr{L}_C = \mathscr{L}_{\mathrm{cl}}(w_1, D_1) + \mathscr{L}_{\mathrm{cl}}(w_2, D_2)$, where [2]

$$\mathscr{L}_{\mathrm{cl}}(w_i, D_i) = exp\left(-2(D_i/2)^2/w_i^2\right). \tag{6}$$

w_i is determined by the cavity geometry, i.e., by the two ROCs R_i and L. In Fig. 7(b), the finesse including the loss model of Eq. (6) was fitted to the data of the PC-MM cavity (solid blue line), leaving $R_{1,2}$ and $D_{1,2}$ as free parameters. The total losses $\mathscr{L}_A + \mathscr{L}_S + \mathscr{T} = 66\,\mathrm{ppm}$ were measured independently by short-cavity finesse measurements (see Eq. (5)) and are used as fixed parameters. In a perfectly symmetric cavity, it would be difficult to attribute clipping loss values to the individual mirrors, since an overestimation of one value could be compensated by the other. Here, due to the slight difference of the ROCs, the beam radius is diverging on the PC fiber mirror for $L < 1650\,\mu\mathrm{m}$ and on the MM mirror for $L > 1650\,\mu\mathrm{m}$, and individual $\mathscr{L}_{\mathrm{cl}}$ values are obtained with good confidence. (To test the reliability of the fit, we have tried to fix D_2 to a value 5% larger than the best fit, and refit the data with this restriction. This lead to an increase of χ^2 by 46%.) The result (solid blue curve in Fig. 7(b)) fits the data well, explaining the sharp drop of $\mathscr{F}$ for $L \sim 1.5\,\mathrm{mm}$ and the decrease for $L \gtrsim 1.8\,\mathrm{mm}$: in these regions, the mode radii on the mirrors $w_{1,2}$ diverge, explaining the decreasing finesse by a rise of the clipping losses. The ROC values $R_{1,2}$ and the effective mirror diameters D_i resulting from the fit are shown in Table 2 together with the ROCs obtained from the 3D optical profilometry of the mirrors. All values agree within the error margins, which shows the reliability of our 3D reconstruction, and confirms that the mirrors are well described by spheres. The initial goal of creating mirror structures with $D_m \approx 100\,\mu m$ is reached for both fiber types. Note that this diameter was chosen to meet our requirements. It was not investigated which maximal diameter the multi-shot method can create.

For the SM-MM cavity, $\mathscr{F}$ drops linearly with increasing L (red dots in Fig. 7(b)). The simple clipping loss model of Eq. (6) does not fit this data with any reasonable parameters. This indicates that the loss is not related to clipping on the mirror edges, but has its origin in

#261274 Received 16 Mar 2016; revised 17 Apr 2016; accepted 18 Apr 2016; published 27 Apr 2016

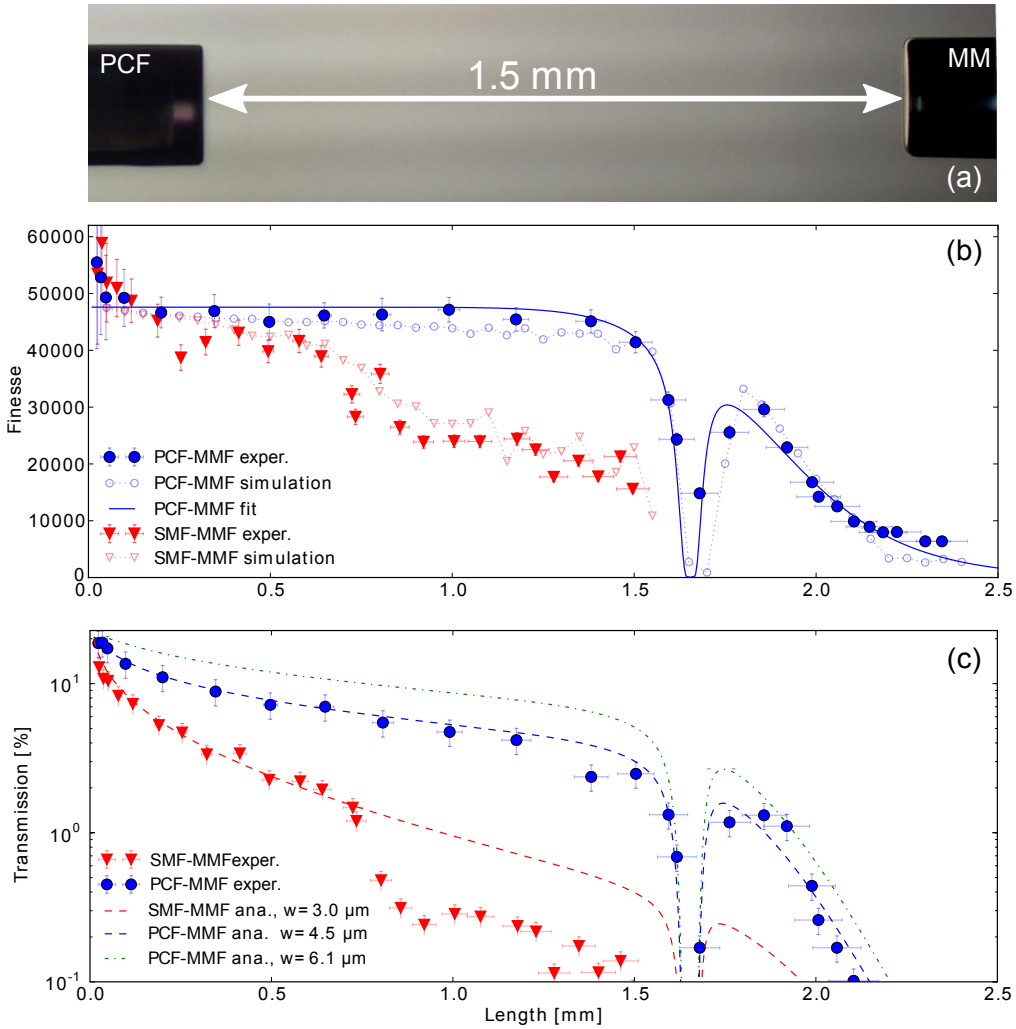

Fig. 7. (a) Microscope image of a fiber Fabry-Perot cavity with a PC fiber (left) and a MM fiber (right). The fibers were illuminated from the back to obtain a high contrast for cavity length measurement. The collapsed region of the PC fiber is visible. (b) Experimental results (filled symbols) and simulations (empty symbols with dotted lines, see 5.3) for the finesse as a function of length. Results are shown for an SM-MM cavity (red triangles) with $R_1 = 1508 \pm 65\,\mu$m and $R_2 = 1629 \pm 73\,\mu$m and for a PC-MM cavity (blue circles) with $R_1 = 1492 \pm 110\,\mu$m and R_2 as before. (The MM fiber is the same in both cavities.) The blue solid line shows the result of the analytical clipping loss formula (6) fitted to the PC-MM data. The fit parameters are given in Table 2. (c) Transmission of the cavities. The PC fiber improves transmission by more than an order of magnitude for $L > 1$ mm. The lines show the calculated transmission using Eq. (7) and the mode field radius w_f given in the legend. $w_f = 6.1\,\mu$m is the mode field radius measured independently for the PC fiber (see Sec. 5.4). The blue dashed line for $w_f = 4.5\,\mu$m fits the PC data well, but the large deviation from the nominal value of the PC mode field radius remains unexplained. The sharp drop in finesse and transmission around $L = 1650\,\mu$m corresponds to the unstable region $R_1 < L < R_2$ of the slightly asymmetric cavity.

#261274 Received 16 Mar 2016; revised 17 Apr 2016; accepted 18 Apr 2016; published 27 Apr 2016

Table 2. **Mirror Diameters and ROCs Deduced from the Finesse Data (see Fig. 7(b))**

	clipping loss model		profilometry[a]
	D_m [μm]	R [μm]	R [μm]
PC (m1)	94	1645$\pm$ 60	1492$\pm$110
MM (m2)	97	1665 $\pm$ 60	1629$\pm$73

[a] ROCs of 2D spherical fits to the mirror profiles.

irregularities of the machined structures shown in Fig. 6. This is confirmed by the numerical simulations which we will now describe.

5.3. Full simulation of the cavity mode using reconstructed mirror surfaces

To gain further insight into the role of structure imperfections, and to be able to predict the performance of the machined structures without building a cavity or even applying a coating, we have performed numerical simulations of the cavity eigenmodes using the measured surface profiles. We have used the FFT toolbox OSCAR [31]. This toolbox simulates cavity eigenmodes for arbitrary mirror profiles, which are represented as 2D arrays of height information. Each of the profiles used in our simulation is the average of 120 profiles of the same fiber taken in succession to reduce noise. Apart from this averaging, no fit or filter was used to process the profile data. The profiles here were taken after coating, but no significant deformation with respect to the profiles of the uncoated structures could be seen.

The simulations covered the full field of view of the profiler (cf. Fig. 4(a)) with a grid resolution of 1.17 μm. The alignment procedure for the simulation is analogous to that of a real cavity: the two profiles are spaced by a fixed distance L, and the resonance closest to the target cavity length is found. By tilting and translating one of the profiles, the transmission signal is optimized. In our simulations, we have not attempted to rotate the profiles around the cavity axis. Their relative angle is left at an arbitrary value and is not changed in the optimization. This is justified when the deviation from rotational symmetry is small, as is the case here. The computation time for a single cavity length, including the alignment procedure, was on the order of one hour on a generic desktop PC. To reach such a reasonable time, the simulations were carried out with higher mirror transmission ($\mathscr{T}_{sim} = 0.01$) compared to the experiment. This has no effect on the simulated clipping and scattering losses of the mirrors. The losses and transmission of the coating, which are not contained in the simulation, are experimentally determined by short-cavity finesse measurements and added to the simulated diffraction losses to determine the finesse using Eq. (5). The results of the simulated finesse are shown in Fig. 7(b) as empty symbols connected by dotted lines for both cavities. Simulation and experiment are in excellent agreement, which confirms that the linear decay of the finesse for the standard single-mode fiber is explained by the structure itself. Additional loss effects from coating variations (as discussed in [11, 32]) are not significant here. Furthermore, this remarkable agreement means that such simulations could be used to optimize structures produced by laser dot milling without laborious iterations of coating and cavity construction.

5.4. Cavity transmission

To compare the measured cavity transmissions to theoretical expectations,we have used the simple model described in [2]. The power coupling efficiency ε between the input fiber and the cavity mode (Eq. (2)) limits the resonant transmission T_c of a symmetric FFP cavity as

$$T_c = \varepsilon \frac{\mathscr{T}^2}{(\mathscr{T} + \mathscr{L})^2}, \tag{7}$$

#261274 Received 16 Mar 2016; revised 17 Apr 2016; accepted 18 Apr 2016; published 27 Apr 2016

where $\mathscr{L} = \mathscr{L}_S + \mathscr{L}_A + \mathscr{L}_C$ is the sum of all mirror losses. (We are assuming that the coupling to the MM output fiber is perfect, which is reasonable because of the large mode area and high acceptance angle of the MM fiber.) The lines in Fig. 7(c) are calculated using this equation. The $\mathscr{T}$ values are the same for all three curves and are those of the multilayer coating (see Sec. 5.2). The length-dependent $\mathscr{L}$ values are deduced from the finesse measurements and take the additional loss with increasing L into account. The coating properties determine the maximum $T_c = 0.207$, achieved for short cavity length. The red dashed line uses the nominal mode field radius $w_f = 3\,\mu$m of the SM fiber and fits the SM-MM data well for lengths up to $L \approx 770\,\mu$m. The sharp drop at this length is not expected from Gaussian mode overlap and could be due to imperfections of the mirror profile discussed above. In that case, optimization of this profile would bring T_c into agreement with the prediction also for larger L. However, this would still be more than five times smaller than the measured T_c of the PC-MM cavity. This confirms the advantage of the PC fiber. Nevertheless, headroom for further improvement remains: indeed, the PC-MM result falls below the expected value if we assume the catalog value for the mode field radius of the PC fiber ($w_f = 8.2\,\mu$m). A good fit is obtained for a much smaller $w_f = 4.5\mu$m (blue dashed line in Fig. 7). To investigate the disagreement more closely, we have measured the mode field radius of the PC fiber independently. The beam profile was imaged with a camera at several distances (1.5 mm - 2.5 mm) from the fiber output, to determine the divergence θ of the beam. By using $w_f = \lambda/(\pi\theta)$, we found $w_f = (6.1 \pm 0.2)\mu$m, significantly smaller than the catalog value. The calculated transmission for this w_f is shown in Fig. 7 (green dash-dotted line), it remains above the measured values. The fact that the PC fiber mode is not strictly Gaussian may explain some of the deviation. To investigate other possible sources, we have tentatively added tilt and displacement in the calculation of ε following [22], but no parameter set could be found which fits the experimental data as well as the model without displacement or angle and $w_f = 4.5\mu$m. Simple propagation of the outcoupled beam in the collapsed part (assumed homogenous) changes the coupling to the cavity mode only slightly and does not explain the difference between theory and experiment. Further possible effects of wavefront distortions, diffraction or lensing at the position of the melted holes of the PC fiber remain to be investigated. Understanding these effects may lead to further improvements of coupling and transmission.

6. Conclusion

These results show that CO_2 laser dot milling and large mode area photonic-crystal fibers form a powerful combination. The maximum length is extended into the millimeter range while maintaining the advantages of a miniature, robust, fiber-based approach and an acceptable overall transmission. Our results also indicate that an improved hole-collapsing process is likely to further improve the transmission. The finesse $\mathscr{F} \sim 50000$ reached in our data is limited by the dual-wavelength coating. The surface roughness of the CO_2 process admits still higher values, and it will be interesting to see whether these can also be reached at the length scale introduced here. For a state-of-the-art single-wavelength coating, total absorption and scattering losses $\mathscr{L}_A + \mathscr{L}_S = 2 \times 13.5$ ppm have been measured for a pair of fiber mirrors [19]. Choosing a transmission of the same value, and adding the clipping losses of 5.5 ppm per mirror estimated by the simulations shown above for a cavity of $L = 1$ mm, it should be possible to produce FFP cavities of $L = 1$ mm and a finesse of up to 97,000 with the method presented here. Beyond the cavity QED applications for which we have originally developed it, we note that the free spectral range for a 1.5 mm fiber cavity is is 100 GHz, approaching an interesting range for filtering applications.

#261274 Received 16 Mar 2016; revised 17 Apr 2016; accepted 18 Apr 2016; published 27 Apr 2016

Acknowledgments

This work was supported by the European Research Council (ERC) (EQUEMI project, GA 671133) and by the EU Information and Communication Technologies programme (QIBEC project, GA 284584). K. O. gratefully acknowledges support from DGA and CNES, and K. S. from the Army Research Laboratory Center for Distributed Quantum Information and FWF. The authors thank Yves Colombe for advice on PC fibers, Tobias Gross of Laseroptik GmbH for the detailed discussions, Nabil Garroum and the ENS Physics Department workshops for machining fiber holders, and Tracy Northup for critical reading of the manuscript.

#261274 Received 16 Mar 2016; revised 17 Apr 2016; accepted 18 Apr 2016; published 27 Apr 2016